International Journal of Heat and Mass Transfer 150 (2020) 119260

Contents lists available at ScienceDirect

International Journal of Heat and Mass Transfer

journal homepage: www.elsevier.com/locate/hmt

Active design for the tube insert of center-connected deflectors based on the principle of exergy destruction minimization

J.Y. Lv, Z.C. Liu, W. Liu*

School of Energy and Power Engineering, Huazhong University of Science and Technology, Wuhan 430074, China

ARTICLE INFO

Article history:
Received 12 March 2019
Revised 18 December 2019
Accepted 19 December 2019
Available online xxx

Keywords:
Center-connected deflector
Longitudinal swirl generator
Active design
Exergy destruction minimization
Multi-objective optimization
Genetic algorithm

ABSTRACT

In this study, a circular tube inserted by center-connected deflector was proposed for heat transfer enhancement, and a numerical simulation with *Re* ranging from 300 to 1500 was conducted to analyze the thermo-hydraulic performance. The results indicated that the insert enhanced heat transfer with an acceptable increase of pressure drop by guiding the fluid from the core to boundary region and generating longitudinal swirl flow with multiple vortexes in the tube. The effects of *Re* and geometrical parameters including pitch (P), inclined angle (α) and deflector diameter (d) were analyzed. When compared to a smooth tube, the Nusselt number was increased by 2.51–9.46 times with the friction factor increasing to 2.48–10.77 times. The thermal dissipation was reduced by 4.82–10.56 times with power consumption increasing to 3.78–12.50 times. Efficiency evaluation coefficient (*EEC*) was in range of 0.92–1.56. Furthermore, a design method was proposed by applying the principle of exergy destruction minimization to determine the optimal geometric parameters of the insert, which was significant for the active design of the tube insert. The multi-objective optimization was performed by genetic algorithm along with artificial neural network. Thermal dissipation and power consumption ratios were chosen as optimization objectives. Then a compromised solution on the Pareto front was obtained. The result indicated that the *EEC* of the optimized structure ($d = 3.63$ mm, $\alpha = 35.85°$, and $P = 67.89$ mm) was 1.32 and that the optimal result based on the principle of exergy destruction minimization had considerable overall performance.

1. Introduction

Thermal energy conversion and transport widely exist in various industrial fields. Since the energy crisis broke out in 1970s, investigations on convective heat transfer enhancement techniques and theories have proliferated to meet the demands of high efficiency of heat exchangers. In general, convective heat transfer enhancement techniques are divided into two categories: passive and active ones. The passive techniques [1,2] are preferred because no extra energy except for pump power consumption for fluid transport is required. Finned tubes, special section tubes, and tube inserts are the main passive techniques for tube-side heat transfer enhancement [3]. Among these methods, tube inserts have advantages in convenient installation and cleaning and are widely applied to realizing specific flow structure.

Based on engineering experiences, modified twisted tapes [4–7], coiled wires [8,9], baffles [10,11], wire mesh [12,13], longitudinal swirl generators [14–17] and other novel tube inserts, such as louvered strip inserts [18] and small pipes insert [19], have been designed and studied numerically or experimentally. Some researchers [20,21] summarized that these inserts mainly enhanced single-phase convective heat transfer by mixing main flow and the flow in the wall region or thinning boundary layer. Zhang et al. [5] conducted numerical studies on heat transfer and flow structure in a tube with multiple regularly spaced twisted tapes and applied physical quantity synergy to analyzing the mechanism for heat transfer enhancement. Guo et al. [6] numerically investigated the thermal-hydraulic characteristics in a circular tube with center-cleared twisted tape by using water as the working fluid, and it was found the thermal performance factor of the tube with center-cleared twisted tape could be enhanced by 7–20% as compared with the tube with conventional twisted tape. Saysroy et al. [7] numerically investigated square-cut twisted tape under turbulent and periodic boundary conditions. The influences of geometries including perforated width to tape width ratios and perforated length to tape width ratios were determined. Feng et al. [8] applied wire coil inserts in microchannel to enhancing heat sink and investigated the effects of different configurations of the inserts numerically and experimentally. Both performance evaluation criteria (PEC) and entropy generation were chosen as performance evaluations. The

* Corresponding author.
E-mail address: w_liu@hust.edu.cn (W. Liu).

https://doi.org/10.1016/j.ijheatmasstransfer.2019.119260
0017-9310/

Nomenclature

a	forepart length of the insert, mm
ANN	artificial neural network
C_p	specific heat capacity, J/(Kg•K)
d	deflector diameter of the insert, mm
e	available potential, J/kg
e_0	available potential at ambient state, J/kg
e_x	thermodynamic exergy, J/kg
D	inner diameter of the tube, mm
EEC	efficiency evaluation coefficient
$E_{xd,\Delta T}$	thermal dissipation, W
$E_{xd,\Delta p}$	power consumption, W
$E_{xd,\Delta T,0}$	thermal dissipation in a smooth tube, W
$E_{xd,\Delta p,0}$	power consumption in a smooth tube, W
f	friction factor
f_0	friction factor of a smooth tube
f_x	local friction factor
h	enthalpy, J/kg
h_0	enthalpy at ambient state, J/kg
h_m	average heat transfer coefficient, W/(m^2•K)
h_r	length in radical direction of the insert, mm
L	length of the tube, mm
MSE	mean square error
n	number for deflector in circumferential direction
$NSGA$	non-dominated sorting genetic algorithm
Nu	Nu number
Nu_0	Nu number of a smooth tube
Nu_x	local Nu number
P	pitch of the insert, mm
Δp	pressure drop, Pa
$\dot{q}$	heat flux, W/m^2
Re	Re number
Reg	Regression coefficient
R_0	radius of the connecting rod, mm
R_t	transitional radius, mm
R	radius of the tube, mm
s	entropy, J/(kg•K)
s_0	entropy at ambient state, J/(kg•K)
r	radial distance, mm
t	thickness of the insert, mm
T	temperature, K
T_w	average temperature of the wall, K
T_m	average fluid temperature, K
T_c	temperature of central point at the inlet, K
T_{in}	temperature at the inlet, K
u	average velocity in the tube, m/s
u_c	velocity of central point at the inlet, m/s
u_{in}	velocity at the inlet, m/s

Greek symbols

α	inclined angle of the insert, (°)
μ	dynamic viscosity of water, kg/(m•s)
ρ	density of water, kg/m^3
λ	thermal conductivity of water, W/(m•k)

heat transfer and pressure drop were experimentally investigated in a tube inserted with equilateral triangle cross sectioned coiled wires in turbulent flow regime by Gunes [9]. The highest overall enhancement efficiency of 36.5% was achieved for the wire with a/D = 0.0892 and $P/D = 1$ at Re number of 3858. Turgut et al. [10] numerically investigated the turbulent forced convection flow and heat transfer characteristics in a tube with baffles. The effects of Reynolds number, baffle angle and baffle distance were analyzed. They concluded that the maximum thermal performance factor was achieved at the baffle angle of 150°. Chang et al. [11] applied periodical oblique baffles and perforated slots for hydrothermal performance improvement and adopted the infrared thermography method to obtain the surface Nusselt number distributions of a square channel. Empirical correlations for average Nu and friction coefficients were devised. Kotresha et al. [12] ultilized local thermal non-equillibrium model to analyze the thermo-hydrolic performance of the brass wire mesh in a vertical channel and acquired the interfacial heat transfer coefficient of the wire mesh porous medium. Tu et al. [13] experimentally investigated the heat transfer performance and pressure drop in a tube with mesh cylinder inserts of different open area rate with Reynold number ranging from 4000 to 18000. They also conducted numerical simulation to analyze the mechanism for heat transfer enhancement. Zheng et al. [14] proposed vortex rods and conducted numerical studies to investigate the thermo-hydraulic characteristics under laminar flow. The inserts were found to work as longitudinal swirl generators and could enhance heat transfer 1.1–3.9 times with pressure drop increasing 1.4–5.3 times. Wang et al. [17] numerically and experimentally investigated the parameters of a novel vortex generators under laminar flow. The results showed that Nu and f were enhanced by 2.55–7.10, 2.21–11.27 times, respectively. Fan et al. [18] employed louvered strip inserts for turbulent airflow and numerically investigated the effects of the slant angle and pitch on the heat transfer, flow resistance and overall performance. Small pipe inserts [19] were proposed by Tu, which were aimed at guiding the fluid in the main region to the wall region and reconstructing the velocity and temperature profile in the tube and thus resulted in a high heat transfer performance. Porous media which could work as tube inserts as well were studied by Tu et al. [22].

In recent years, with the development of optimize algorithm theory and computer technology, optimization algorithm such as genetic algorithm [23] coupled with surrogate models such as artificial neural networks [24] have been applied in various fields, such as medicine, data fitting and clustering in engineering, to provide optimal solutions for complex problems. In the field of heat transfer enhancement technology, some researchers [15,16] have paid attention to conduct optimization for structure parameters by optimize algorithm. Abdollahi et al. [15] utilized CFD soft to simulate heat transfer and flow structure of winglet vortex generator in a rectangular channel and then optimized geometrical parameters by genetic algorithm along with artificial neural network. Zheng et al. [16] conducted the analogous research method with Abdollahi's to obtain optimal parameters for the vortex rod insert. Their optimization objectives were Nusselt number ratio and friction factor ratio.

The existing enhanced heat transfer techniques were mainly proposed based on engineering experiences. The essence of the convective heat transfer enhancement was still unclear in 1990s. Theories and principles for heat transfer enhancement technology were developed to reveal the mechanism and provide guidance for high efficiency without excessive pressure drop. Bejan et al. [25,26] proposed entropy generation minimization principle, which introduced thermodynamic optimization, second-law analysis and thermodynamic design into a heat transfer process for the first time. They obtained an expression for entropy generation caused by heat transfer and fluid friction. Guo et al. [27,28] proposed a new physical quantity named entransy which described heat transfer ability and developed entransy dissipation extreme principle which mainly focused on heat transfer phenomena. Zhao et al. [29] conducted a collaborative optimization method for heat transfer systems based on the heat current method and entransy dissipation extremum principle. Wang et al. [30] conducted entropy and entransy analyses of Rankine cycle and concluded that larger entransy loss rate related to larger output power, while smaller entropy generation rate did not. In addition, Guo et al. [31,32] put

forward and developed field synergy principle which provided a way to strengthen heat transfer theoretically. Some researchers [33,34] applied the principle to analyzing and evaluating the heat transfer effect of certain techniques according to the degree of synergy between the temperature and velocity fields. Based on the field synergy principle, Liu et al. [35–38] further proposed multi-field synergy principle and obtained the relations among velocity, pressure, temperature and component concentration according to the synergy equations. Cao et al. [39] extended field synergy to analyze the noise propagation process by establishing relationships between the flow and pressure gradient fields. Moreover, Liu et al. [40] proposed the concept of available potential and exergy destruction minimization. Both thermal dissipation and power consumption were taken into account completely. An optimized flow field was obtained by Wang et al. [41] according to exergy destruction caused by heat transfer.

In this paper, enlightened by previous investigations on tube inserts, a novel tube insert is proposed for heat transfer enhancement in a circular tube to concretely realize longitudinal swirling flow which is found to be optimal flow field by solving optimization equations [37]. Furthermore, the present work is aimed to combine the principle of exergy destruction minimization proposed in Ref. [36] and industrial practice by putting forward a feasible method for the optimization to apply the principle to the active design of geometrical parameters of tube inserts. The optimal design aims at efficient heat transfer enhancement without excessive pressure drop by collaboratively minimizing the exergy destructions caused by heat transfer and fluid flow.

2. Exergy destruction minimization

Liu et al. [36] proposed the concept of available potential to describe the effective transfer of thermal energy by taking both the unavailability of thermal energy and the irreversibility of a transfer process into account. The available potential was defined as

$$e = h - T_0 s, \tag{1}$$

where h is enthalpy, T_0 is ambient temperature, and s is entropy. The first part on the right hand h represents the total potential of working fluid, and the second part $T_0 s$ represents the unavailable thermal potential. It means that only thermal energy above ambient temperature can be utilized in a heat conversion or transfer process. The available potential represents the energy potential of a working fluid that is available to do work. There are difference and connection between available potential and thermodynamic exergy, which is defined as

$$e_x = (h - T_0 s) - (h_0 - T_0 s_0) = e - e_0, \tag{2}$$

where h_0, s_0 and e_0 are enthalpy, entropy and reference potential at ambient state, respectively. According to Eq. (1), the total derivative of available potential for an uncompressible fluid can be expressed as [36],

$$\rho \frac{De}{Dt} = \rho (T - T_0) \frac{Ds}{Dt} + \frac{Dp}{Dt}. \tag{3}$$

The total derivative expression of entropy and pressure are shown as follows,

$$\rho \frac{Ds}{Dt} = -\nabla \cdot \frac{\boldsymbol{q}}{T} + \frac{\Phi}{T} + \frac{\lambda (\nabla T)^2}{T^2}, \tag{4}$$

$$\frac{Dp}{Dt} = \boldsymbol{U} \cdot \nabla p = -\boldsymbol{U} \cdot (\rho \boldsymbol{U} \cdot \nabla \boldsymbol{U} - \mu \nabla^2 \boldsymbol{U}), \tag{5}$$

where q is the heat flux vector, Φ is viscous dissipation function, λ and μ are thermal conductivity and dynamic viscosity of fluid, respectively. By substituting Eqs. (4) and (5) into Eq. (3), the total derivative expression of available potential is obtained as follows,

$$\rho \frac{De}{Dt} = -\nabla \cdot \left[\left(1 - \frac{T_0}{T}\right) \boldsymbol{q} \right] + \left(1 - \frac{T_0}{T}\right) \Phi - \frac{\lambda T_0 (\nabla T)^2}{T^2} - \boldsymbol{U} \cdot (\rho \boldsymbol{U} \cdot \nabla \boldsymbol{U} - \mu \nabla^2 \boldsymbol{U}). \tag{6}$$

The first term at the right hand is defined as exergy flux caused by heat transfer through the boundary. The second term is heat exergy caused by viscous heat. According to the results of our calculation, the error by not accounting for viscous dissipation is below 0.01%. Therefore, it is reasonable to neglect the heat exergy caused by viscous heat. The last two terms are exergy destruction rates caused by heat transfer and fluid flow, which can characterize irreversibility of a convective heat transfer process.

According to Gauss' divergence theorem, the total exergy flux entering in the computational domain Ω can be obtained by integrating on the boundary region Γ, which is written as:

$$E_x = \iiint_{\Omega} -\nabla \cdot \left[\left(1 - \frac{T_0}{T}\right) \boldsymbol{q} \right] dV = \oiint_{\Gamma} -\boldsymbol{q_e} \cdot d\boldsymbol{S}. \tag{7}$$

The exergy destruction rate caused by heat transfer corresponds to thermal dissipation owing to temperature differences, and exergy destruction rate caused by fluid flow corresponds to power consumption owing to pressure drop. Integrated in the computational domain Ω, the total exergy destruction can be expressed as

$$E_{xd} = \iiint_{\Omega} \left[\frac{\lambda T_0 (\nabla T)^2}{T^2} + \boldsymbol{U} \cdot \left(\rho \boldsymbol{U} \cdot \nabla \boldsymbol{U} - \mu \nabla^2 \boldsymbol{U} \right) \right] dV, \tag{8}$$

or

$$E_{xd} = E_{xd,\Delta T} + E_{xd,\Delta p}. \tag{9}$$

The larger the exergy destruction is, the higher the degree of irreversibility in a heat transfer process will be. When the thermal dissipation is smaller, it means that the temperature distribution of the fluid is more homogenous. When the power consumption is smaller, it means that the pressure drop of the fluid is reduced. Therefore, the target for efficient heat transfer enhancement with low pressure drop can be achieved by collaboratively minimizing the thermal dissipation and power consumption to reduce the irreversibility of heat transfer and fluid flow. Recently, Liu [36] et al. proposed a principle designated as exergy destruction minimization and obtained an optimized flow field of convective heat transfer in a circular tube. The longitudinal whirl flow with multiple vortexes was found as the optimum flow field by solving the optimization equations derived by the method of functional variation [37], which provided a guide to design the insert in a circular tube. In this study, however, we aim to develop a method to design the insert based on the principle of heat transfer enhancement through minimizing exergy destruction of the fluid displayed in Eq. (8).

3. Geometrical model

The physical model of a heat transfer enhanced tube fitted with a center-connected inclined deflector are shown in Fig. 1. According to the experiences in previous researches and trial calculation before formal calculation, the parameters such as pitch (P), inclined angle (α), and deflector diameter (d) have greater influences on heat transfer enhancement and flow structure than other parameters such as diameter for center rod, thickness, etc. Therefore, only the effects of deflector diameter, inclined angle, and pitch are investigated numerically.

The length (L) of computational domain is 500 mm, which is large enough to capture the regular characteristics in the rear part of tube. The inner diameter (D) of the tube is 20 mm. An upstream section without deflectors is set at the front part of the tube to

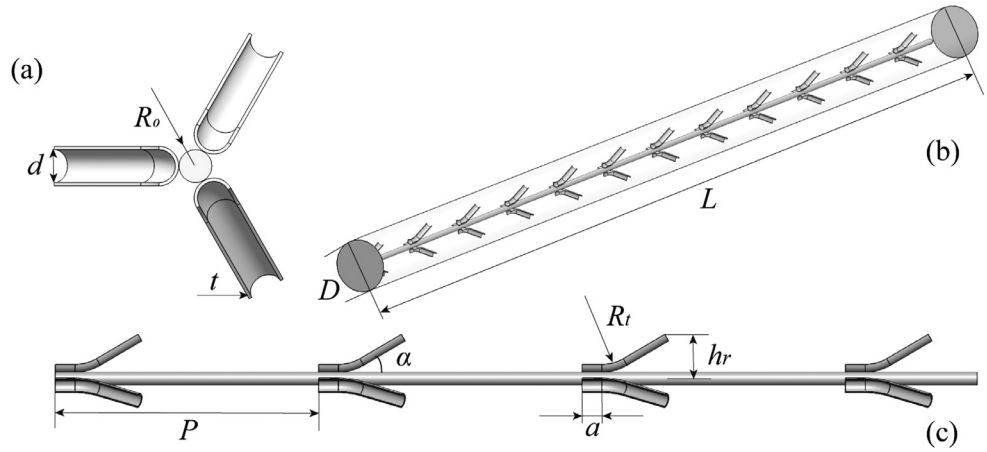

Fig. 1. A geometrical model of heat transfer tube: (a) deflector; (b) enhanced tube with inserts; and (c) center-connected inclined deflectors.

Table 1
Geometrical parameters of the tube and inserts.

L, mm	D, mm	R_0, mm	a, mm	R_t, mm
500	20	1	3	5
h_r, mm	t, mm	d, mm	α, °	P, mm
9	0.2	2, 2.5, 3, 3.5, 4	20, 30, 40, 50, 60	30, 40, 50, 60, 70

satisfy the continuity for Eqs. (13) and (14) at the inlet of the tube. The length of the upstream section to ensure fully developed conditions at the inlet is set to 5 mm. Liu et al. [45] have investigated the number for strips in the circumferential direction. They have found that f/f_0 is more sensitive to the increasing of number for conical strips than Nu/Nu_0, which indicates that the overall performance decreases with the increasing number for strips. In addition, supposing the number for deflectors is two or less, the full mixing of fluid cannot be guaranteed. Therefore, a moderate number for deflectors ($n = 3$) in the circumferential direction is fixed. The radius of the central rod (R_0), to which three deflectors are circumferentially connected, is 1 mm. The geometrical parameters of the deflectors are as follows: a forepart length (a) of 3 mm and a transitional radius (R_t) of 5 mm are set to guide the fluid smoothly; the length in the radial direction (h_r) is fixed to 9 mm; the thickness (t) of the deflectors is fixed to 0.2 mm. Five values for deflector diameter (d), inclined angle (α), and pitch (P) are chosen respectively in the numerical calculation. These parameters are listed in Table 1.

4. Numerical simulation

4.1. Governing equations and boundary conditions

In the present work, water is selected as working medium, which is considered as Newtonian incompressible fluid. Reynolds numbers are in range of 300–1500. Since the temperature range is limited, the effect of radiation is neglected, and the physical properties of the fluid are constant. In addition, due to a small-size tube positioned horizontally, the effect of gravity is neglected. The model is assumed to be three-dimensional and steady-state. Viscous dissipation is not considered. Based on the assumptions above, the governing equations for the mass, momentum and energy conservations are introduced as follows,

$$\frac{\partial u_i}{\partial x_i} = 0, \tag{10}$$

$$\frac{\partial}{\partial x_j}\left(\rho u_i u_j\right) = -\frac{\partial p}{\partial x_i} + \frac{\partial}{\partial x_j}\left[\mu\left(\frac{\partial u_i}{\partial x_j} + \frac{\partial u_j}{\partial x_i}\right)\right], \tag{11}$$

$$\frac{\partial}{\partial x_i}\left(\rho u_i c_p T - \lambda\frac{\partial T}{\partial x_i}\right) = 0,\ (i,\ j = 1, 2, 3), \tag{12}$$

where ρ is the density of water, u_i is the velocity component in the x_i direction, μ is the dynamic viscosity, c_p is the specific heat, and λ is the thermal conductivity.

A constant heat flux (2000 W/m^2) is applied to the no-slipping tube wall. As shown in Eqs. (13) and (14), the fully developed velocity and temperature boundary conditions are set at the inlet of the tube.

Inlet temperature condition:

$$T_{in} = T_c + \frac{\dot{q}R_0}{\lambda}\left[\left(\frac{r}{r_0}\right)^2 - \frac{1}{4}\left(\frac{r}{r_0}\right)^4\right], \tag{13}$$

Inlet velocity distribution:

$$u_{in} = u_c\left[1 - \left(\frac{r}{r_0}\right)^2\right], \tag{14}$$

where r_0 is the tube radius, and r is the radial distance. T_c and u_c are the temperature and velocity of the central point at the inlet, respectively. $\dot{q}$ is the heat flux applied to the wall.

An outflow boundary condition is adopted to the outlet of the tube. In this study, FLUENT 16.0 software based on the finite volume method is employed to solve the governing equations with boundary conditions. The coupling of pressure and velocity is achieved by the SIMPLE algorithm. The convergence criteria are less than 10^{-6} for the continuity and momentum equations and 10^{-8} for the energy equation.

4.2. Data reduction

According to the calculation results, the Reynolds number (Re), average heat transfer coefficient (h_m), friction factor (f), Nusselt number (Nu), efficiency evaluation coefficient (EEC), thermal dissipation ($E_{xd,\Delta T}$), power consumption ($E_{xd,\Delta p}$) of the fully developed section and the ratios of them are obtained as follows.

The Reynolds number (Re), which characterizes the relative influences of inertial and viscous forces in a fluid problem, is calculated by

$$\mathrm{Re} = \frac{\rho u_m D}{\mu}, \tag{15}$$

where u_m is the mean velocity of the flow direction.

The average heat transfer coefficient h_m, which characterizes the amount of heat transferred in an area of 1 m*1 m per second when the temperature difference between the solid wall and fluid is 1 K, is calculated by

$$h_m = \frac{\dot{q}}{T_w - T_m}, \tag{16}$$

where T_w and T_m are the average wall temperature and average fluid temperature of the fully developed section, respectively.

The Nusselt number (Nu), which indicates the strength of convective heat transfer, is defined as

$$Nu = \frac{h_m D}{\lambda}, \tag{17}$$

and the friction factor, which is related to the total pressure drop in a tube, is given by

$$f = \frac{\Delta p}{(1/2\rho u^2)(z/D)}, \tag{18}$$

where Δp and z are the pressure drop and tube length of the chosen section.

$$EEC = \frac{Nu/Nu_0}{\Delta p/\Delta p_0} \approx \frac{Nu/Nu_0}{f/f_0}, \tag{19}$$

where Nu_0, f_0, and Δp_0 are the Nusselt number, friction factor, and pressure drop in a smooth tube, respectively. Obviously, EEC characterizes the ratio between the benefits of heat transfer enhancement and the cost of increasing power consumption. Therefore, $EEC > 1$ is expected which indicates profitability, while $EEC < 1$ should be avoided.

In addition, the thermal dissipation $E_{xd,\Delta T}$ and power consumption $E_{xd,\Delta p}$, i.e., the exergy destructions caused by heat transfer and fluid flow, are obtained as follows [36],

$$E_{xd,\Delta T} = \iiint_{\Omega} \frac{\lambda T_0 (\nabla T)^2}{T^2} dV, \tag{20}$$

$$E_{xd,\Delta p} = \iiint_{\Omega} \boldsymbol{U} \cdot \left(\rho \boldsymbol{U} \cdot \nabla \boldsymbol{U} - \mu \nabla^2 \boldsymbol{U}\right) dV. \tag{21}$$

The thermal dissipation and power consumption in a smooth tube are constant and are denoted as $E_{xd,\Delta T,0}$ and $E_{xd,\Delta p,0}$, respectively. The thermal dissipation ratios (TDR for short) and power consumption ratios (PCR for short) are defined as

$$TDR = \frac{E_{xd,\Delta T,0}}{E_{xd,\Delta T}}, \tag{22}$$

$$PCR = \frac{E_{xd,\Delta p}}{E_{xd,\Delta p,0}}. \tag{23}$$

Table 2
Grid independence test.

Grid system	Cells number	*Nu*	Error-*Nu*	*f*	Error-*f*
1	5542364	20.06537	6.7%	0.361273	2.10%
2	10343385	19.10011	1.6%	0.368072	0.26%
3	15461209	18.80377	–	0.369038	–

Evidently, TDR characterizes the reduction in the thermal dissipation of the heat transfer enhanced tube when compared to the smooth tube, and PCR indicates the increase in power consumption.

4.3. Mesh generation and accuracy verification

Before the numerical simulation, mesh independence test and accuracy verification are conducted. ICEM 16.0 is utilized to generate three-dimensional mesh systems. As presented in Fig. 2, a hybrid grid system consisting of prism grids, tetrahedral grids, hex cores and pyramids is generated in the flow area. To capture the accurate characteristics of the flow structures and heat transfer in the boundary layer, the mesh near the wall is particularly refined. A tube fixed with the insert with the pitch of 30 mm, deflector diameter of 2 mm and inclined angle of 40° is chosen to generate three different mesh systems (5542364, 10343385, and 15461209 elements respectively). As shown in Table 2, the relative errors for Nusselt number and friction factor between system 3 and system 2 are 1.6% and 0.26%, respectively. It indicates that mesh settings for system 2 is dense enough to meet the calculative accuracy requirements. In addition, since grid number for system 3 is about 1.5 times larger than system 2, calculation resources can be saved with system 2. Therefore, mesh settings for system 2 are adopted in our study.

A numerical simulation is conducted in a smooth circular tube to further prove the credibility of the simulation results. The comparison results of the Nusselt number and friction factor between the computational and theoretical values of fully developed laminar flow are shown in Fig. 3. The largest deviations between the numerical and theoretical values are 2.7% for the Nusselt number and 1.6% for the friction factor. Considering the transition of laminar flow may be arisen in some cases of this study, the SST k-ω turbulence model which provides modifications for low Reynolds number effects is applied in several cases to further prove the applicability of laminar flow model. Five cases with largest deflector diameter and inclined angle are calculated by laminar model and SST k-ω turbulence model with Re fixed to 1500 respectively. As illustrated in Fig. 4, the largest deviations for Nu and f between

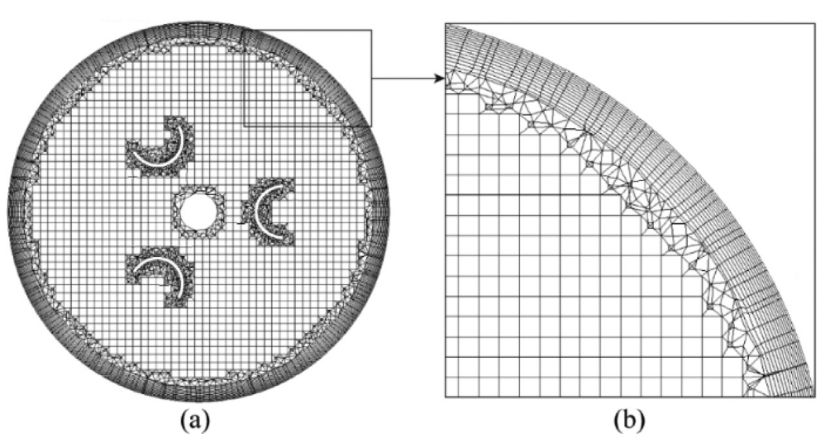

Fig. 2. Mesh generation for a tube with center-connected inclined deflector.

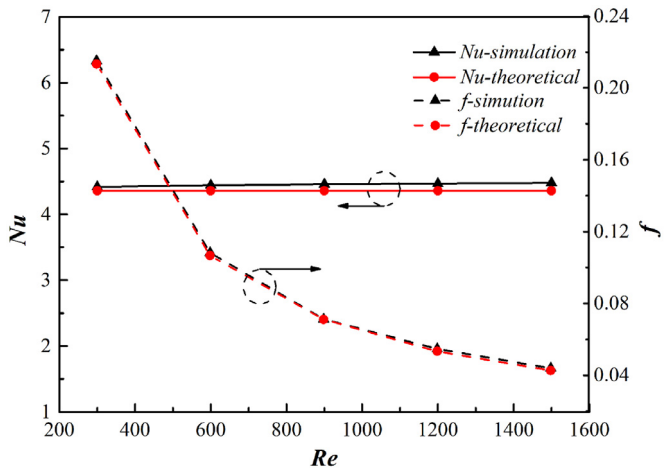

Fig. 3. Comparisons between numerical results and theoretical values for smooth tube.

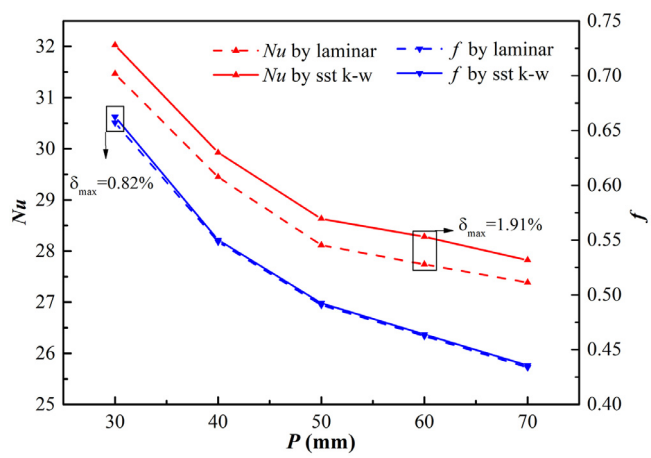

Fig. 4. Comparison between the numerical results calculated by laminar model and SST k-ω model.

the two models are 1.91% and 0.82%, respectively. Therefore, it is concluded that the numerical results are considered reliable.

5. Results and discussion

5.1. Thermal-hydraulic characteristics

5.1.1. Heat transfer enhancement mechanism

As shown in Fig. 5, there is a great difference between the temperature contours at the outlet of a heat transfer enhanced tube

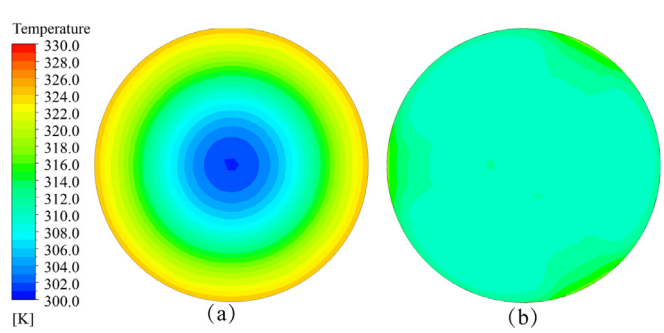

Fig. 5. Temperature contours: (a) at outlet of a smooth tube and (b) at outlet of an enhanced tube (P = 60 mm, α = 30°, d = 2.5 mm, Re = 900).

and that of a smooth tube. In the enhanced tube, the temperature profile is more homogenous at the outlet owing to the center-connected inclined deflectors. According to the computational results, with d in range of 2–4 mm, P of 30–70 mm, α of 20° to 60° and Re of 300–1500, when compared with a smooth tube, heat transfer of fully developed section in the tube with the investigated insert is enhanced by 2.51–9.46 times, while the pressure drop is increased by 2.48–10.77 times.

To investigate the mechanism for heat transfer enhancement in the tube, the temperature profiles and velocity distributions in the cross and axial section of the tube with the insert with the pitch of 60 mm, inclined angle of 30° and deflector diameter of 2.5 mm are exhibited in Figs. 6 and 7. There are two main reasons accounting for the heat transfer enhancement. On the one hand, the tube inserts can work as longitudinal swirl generators. As presented in Fig. 6 (a), velocities perpendicular to the mainstream are produced, which contribute to the mixing of heated water near the wall and cold water in the core region. As shown in Fig. 6 (b), three pairs of longitudinal vortexes are generated in the entire fluid region, which are helpful in lengthening the flow path and thus make the water heated more adequately. The strength of vortex is weakened behind the inserts and strengthened again periodically. On the other hand, the inserts can work as deflectors. The temperature distribution of the axial section is displayed in Fig. 7. It is evident that the cold water in the core region is deflected to the boundary region. In addition, water is guided to scour the tube wall intensively and the boundary layer has been broken. Thus, the heat transfer is enhanced due to the effect of deflecting flow caused by the deflectors.

As shown in Fig. 8 (a) and (b), it is visible that both local average Nu and f are much higher than that of a smooth tube and seesaw along the mainstream direction. The deflectors periodically strengthen heat transfer and disturb flow field in the tube, which contributes to the periodic oscillations of local Nusselt number and friction factor. The maximum local Nu occurs exactly at the posterior surface of the periodically arranger deflector due to the vortexes induced, while the maximum friction factor occurs at the front surface due to the frontal impact of fluid. Moreover, different geometrical parameters lead to the similar law of variations but different level for local Nusselt number and friction factor. In addition, it is indicated that there are two stages of heat transfer in the tube, the developing and fully developed stage. In the developing stage, the first several deflectors cause great change on the temperature profile in the front section, which corresponds to the irregular distributions of Nu_x with $z < 200$ mm in the Fig. 8(a). In the fully developed stage, deflectors equidistantly inserted in the rear end of the tube further lead to stable heat transfer enhancement pattern and thus periodically regular oscillations of Nu_x in $z > 200$ mm section.

5.1.2. Exergy destruction and convective heat transfer

As presented in Eqs. (22) and (23), we can define a ratio of thermal dissipation between the smooth tube and enhanced tube, and a ratio of power consumption between the enhanced tube and smooth tube. The former can represent the decreasing amplitude of exergy destruction caused by heat transfer, and the latter can represent the increasing amplitude of exergy destruction caused by fluid flow in the fully developed section of enhanced tube. With d in range of 2–4 mm, P of 30–70 mm, α of 20° to 60° and Re of 300–1500, when compared with a smooth tube, the thermal dissipation in a heat transfer enhanced tube is decreased by 4.82–10.56 times, while the power consumption is increased by 3.78–12.50 times.

The numerical calculation, in which the deflector diameter is fixed to 3.5 mm and Re to 900, is conducted to exhibit the exergy destruction ratios. Fig. 9 shows the variations of thermal dis-

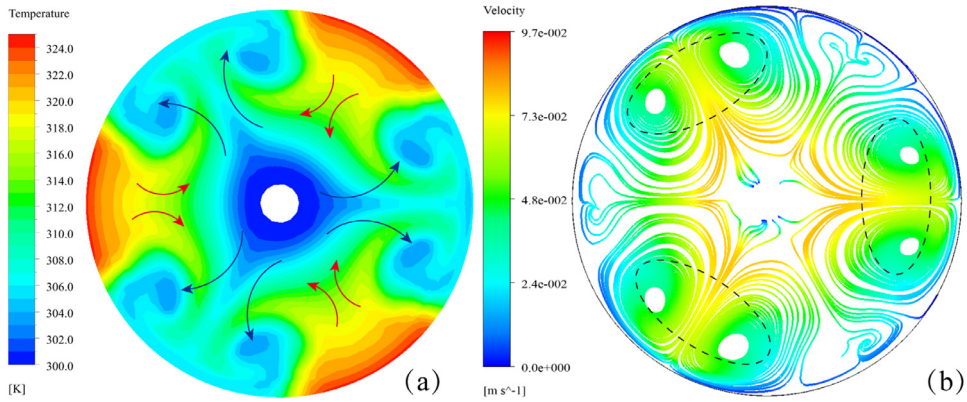

Fig. 6. Temperature contour and streamline on plane at z = 40 mm (P = 60 mm, α = 30°, d = 2.5 mm): (a) temperature distribution; (b) longitudinal swirls generated in tube.

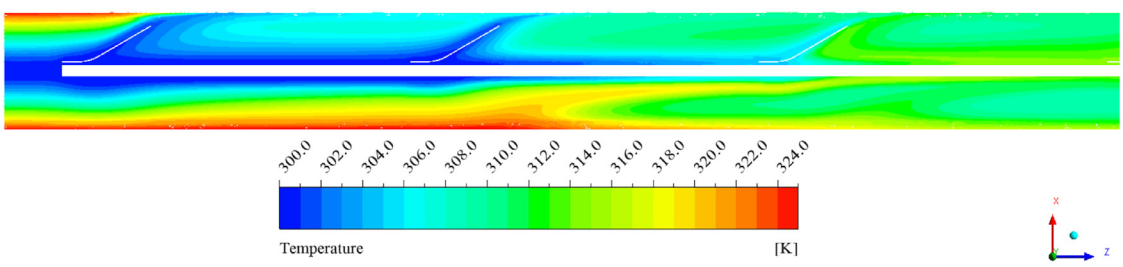

Fig. 7. The effect of deflecting flow caused by deflectors (P = 60 mm, α = 30°, d = 2.5 mm): temperature contour in axial section (from z = 0 mm to z = 200 mm).

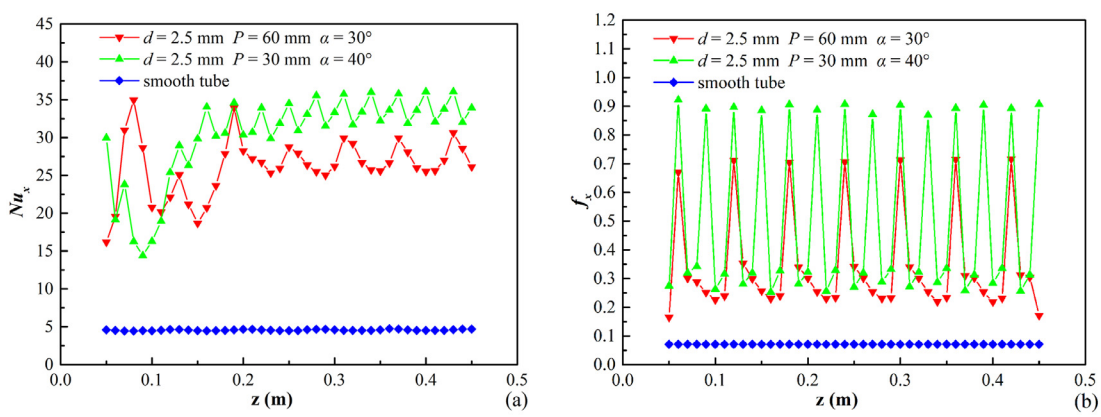

Fig. 8. Local Nusselt number and friction factor along the z-axis direction:(a) Nu_x and (b) f_x.

sipation ratios and Nusselt number ratios, and Fig. 10 presents the variations of power consumption ratios and friction factor ratios. It is found that there are associations between the exergy destruction related to thermal dissipation and power consumption and convective heat transfer characterized by Nu and f. On the one hand, the temperature distributions of fully developed section in the enhanced tube become more homogenous than that of a smooth tube owing to heat transfer enhanced by the inserts. Therefore, the thermal dissipation in an enhanced tube is reduced. The larger the increase amplitude of Nusselt numbers, the larger the decrease amplitude of thermal dissipation. On the other hand, the velocity perpendicular to the main flow generated owing to the inserts leads to momentum loss in the tube, which results in a similar increasing trend of the friction factor and power consumption.

5.2. Effect of geometrical parameters

5.2.1. Effect of the inclined angle

Five values of 20°, 30°, 40°, 50°, 60° for the inclined angle are taken into account to investigate the thermal-hydraulic characteristics. With the deflector diameter fixed to 3.5 mm and Reynolds number fixed to 900, the Nusselt number and friction factor ratios (Nu/Nu_0 and f/f_0) of fully developed stage varied with the inclined angles under serial pitches are shown in Figs. 9 and 10. The EEC values are illustrated in Fig. 11. It is evident that Nu/Nu_0 and f/f_0 are both larger than 1, which means that heat transfer is enhanced at the cost of increase in friction factor. As shown in Fig. 9, when the pitches are small, the Nusselt number ratios increase with the increase in the inclined angles. When the pitches are large enough,

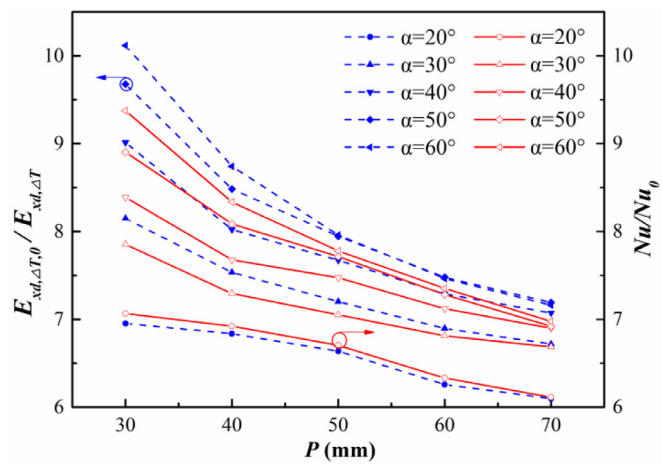

Fig. 9. Variation ratios of exergy destruction (blue dotted curves) of heat transfer and *Nu* number (red solid curves) with *P* at $d = 3.5$ mm and $Re = 900$. (For interpretation of the references to color in this figure legend, the reader is referred to the web version of this article.)

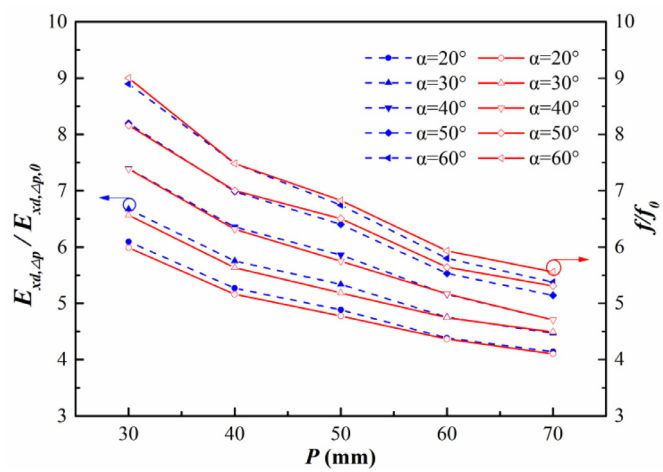

Fig. 10. Variation ratios of exergy destruction (blue dotted curves) of fluid flow and *f* (red solid curves) with *P* at $d = 3.5$ mm and $Re = 900$. (For interpretation of the references to color in this figure legend, the reader is referred to the web version of this article.)

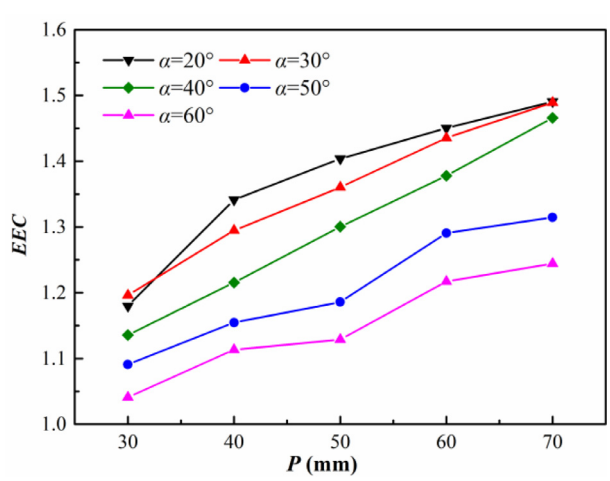

Fig. 11. Variations of the *EEC* with inclined angle under different pitches at $d = 3.5$ mm, $Re = 900$.

the inclined angle has little influence on Nusselt number ratios. As shown in Fig. 10, the friction factor ratios always increase with the increase in the inclined angle. The *EEC* value decreases with the increase in the inclined angle.

Temperature and velocity field distributions for different inclined angles with $Re = 900$, $d = 2.5$ mm, $P = 60$ mm are illustrated in Fig. 12. It is evident that the inclined angles have a great influence on the effect of scouring wall. The deflectors with larger inclined angles guide the water to scour the wall more intensively, which leads to larger Nusselt numbers. Consequently, as shown in Fig. 12 (a), the temperature profile is more uniform with larger inclined angle. When the pitches are large enough, the changes in vortex strength related to the pitches are more dominant than the scouring effects related to the inclined angles. Therefore, with the increasing in inclined angle, there are little variation in Nusselt number. In addition, the inserts with larger inclined angles lead to more momentum loss of the fluid, which increases the friction factor and power consumption.

5.2.2. Effect of the pitch

The Nusselt number and friction factor ratios with five values for pitches at serial inclined angles at $d = 3.5$ mm and $Re = 900$ are displayed in Figs. 9 and 10. It is evident that *Nu* number and friction factor ratios both decrease with the increase in the values for pitch. With the inclined angles fixed to 30° and the deflector diameters fixed to 2.5 mm, Fig. 13 (a) and (b) show the temperature contours of the axial cross section and swirling strength in the tube, respectively. It is found that each deflector has a great impact on the heat transfer and flow characteristics in the posterior zone. The impact is weakened in the region behind each deflector and is strengthened again when water flows past the next deflector. Smaller pitches allow more deflectors in the fixed length, which makes the turbulence strengthened more frequently. Moreover, as shown in Fig. 13 (b), the area affected by the swirling flow is much broader with more inserts in the tube. As shown in Fig. 13 (a), the temperature becomes more homogenous with smaller pitches. However, it demonstrates that more center-connected inclined deflectors in the tube with fixed length lead to more flow blockages, which leads to larger pressure drop in the tube. Therefore, it is critical to choose the appropriate value for pitch according to the specific requirements.

5.2.3. Effect of the deflector diameter

With the inclined angle fixed to 40° and the pitch fixed to 70 mm, variations of the *Nu* number ratios and friction factor ratios of fully developed section with different deflector diameters and Reynolds numbers are shown in Fig. 14. The *EEC* values varied with the *Re* numbers and deflector diameters are presented in Fig. 15. As the *Re* number increases, both the *Nu* number and friction factor ratios increase enormously at a given deflector diameter. Both increase with the increase in the deflector diameter when the *Re* numbers are in the range of 300–1500. It is found that when *d* is in range of 2–4 mm, a larger value for *d* will lead to better effect of heat transfer enhancement with *Re* in range of 300–1500. In addition, when *Re* is in range of 300–1200, the *EEC* decreases with the increase in *d*. When *Re* is 1500, the *EEC* is few influenced by *d*.

Fig. 16 illustrates the velocity component perpendicular to the main direction in the cross sections behind the deflectors with $Re = 900$, $\alpha = 30°$, $P = 40$ mm to analyze the impact effects of the deflector diameters. Nonetheless, the velocity in the core region near the deflector is not low since the velocity in the main direction should be involved as well. It is evident from the velocity distributions that the defectors with larger deflector diameters guide more water from the core region to scour the wall. The larger deflector diameter means a wider projected area in the transverse

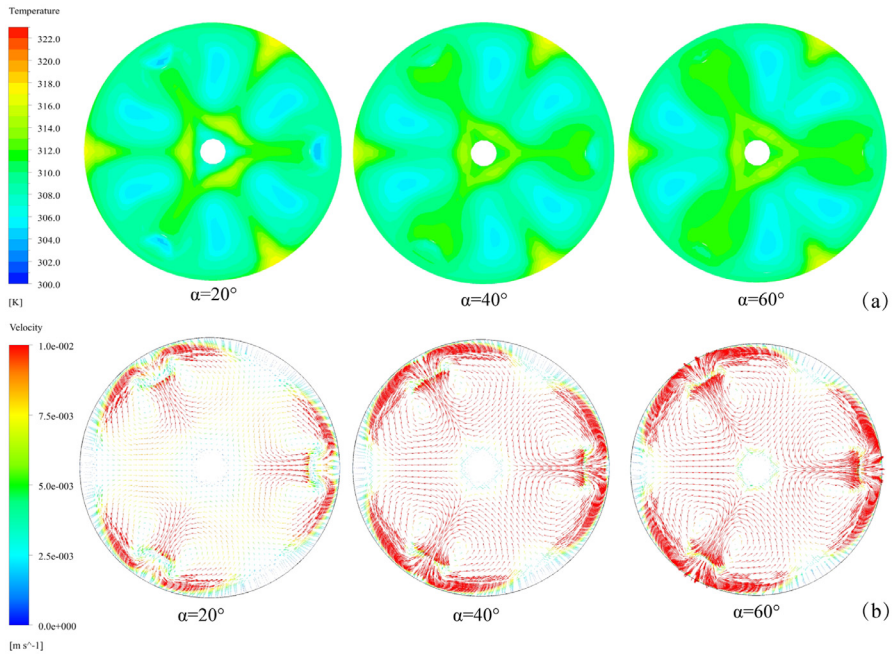

Fig. 12. Temperature and velocity field behind a deflector in the tube with $Re = 900$, $d = 2.5$ mm, $P = 60$ mm: (a) temperature contours; (b) velocity distributions.

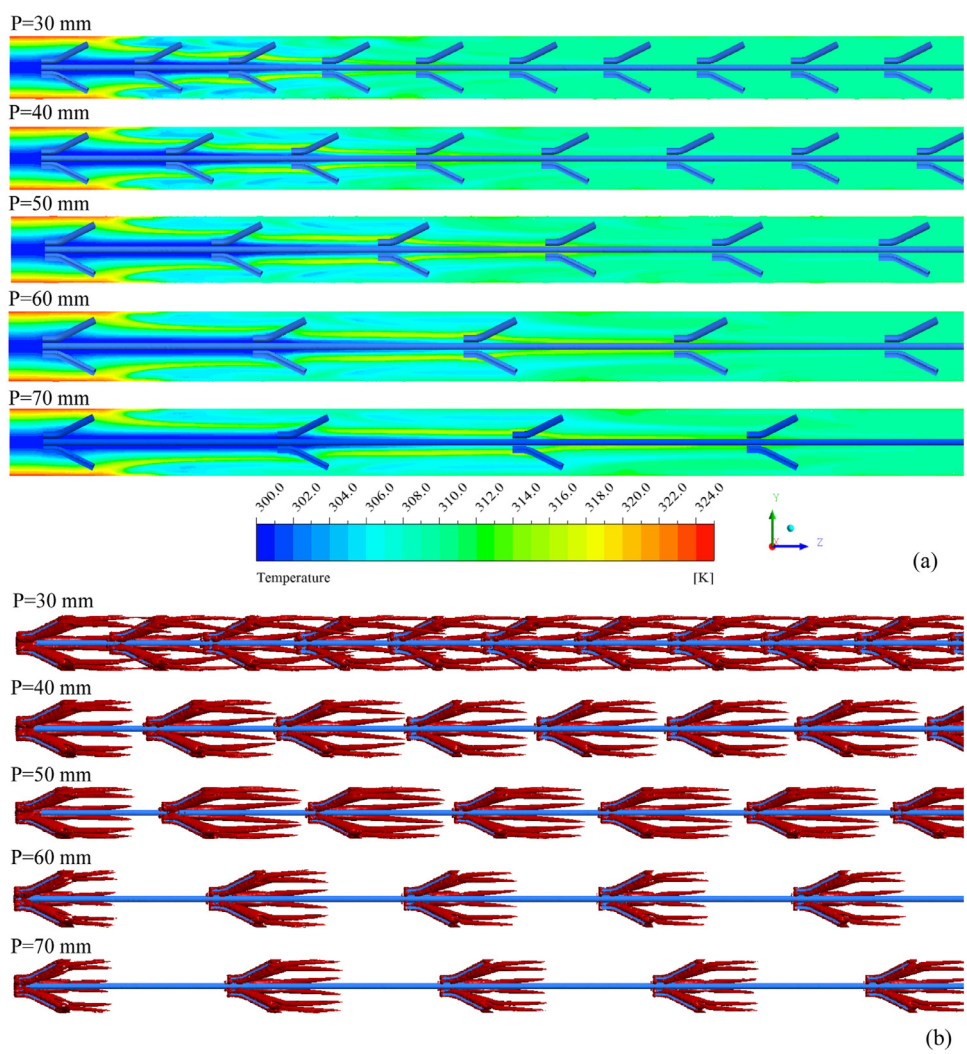

Fig. 13. (a) Temperature contours of axial cross section and (b) vortex core region in tube with $d = 2.5$ mm and $\alpha = 30°$.

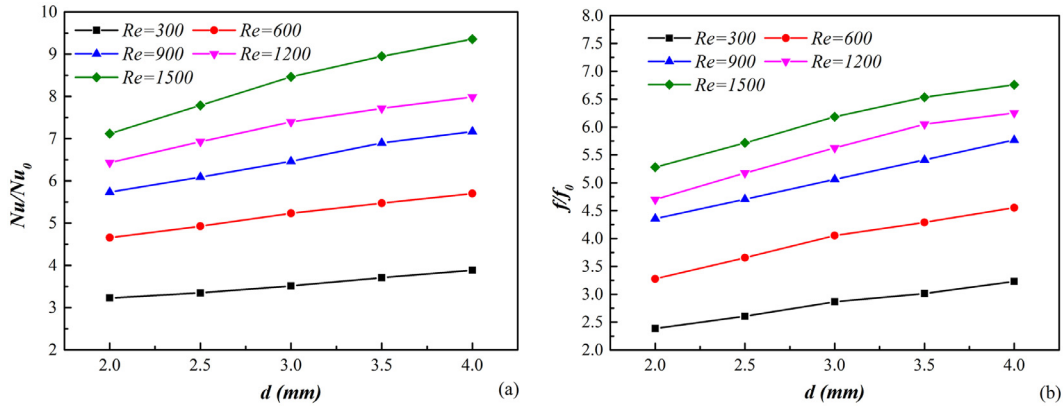

Fig. 14. Variations of Nu/Nu_0 and f/f_0 with deflector diameter at $\alpha = 40°$, $P = 70$ mm: (a) Nu/Nu_0, and (b) f/f_0.

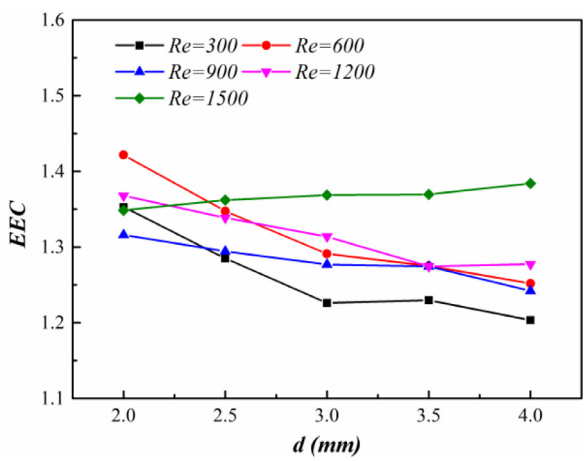

Fig. 15. EEC value varied with *Re* number and deflector diameter at $\alpha = 40°$, $P = 70$ mm.

plane. The region disturbed by the inserts with $d = 4$ mm is the widest. Besides, inserts with large deflector diameters lead to severe turbulence and full mixing in the tube. However, as the deflector diameter increases, more working fluid is deflected to change the initial flow direction, and the velocity perpendicular to the main flow is generated more significantly. Therefore, more momentum loss in the mainstream direction is caused, which results in an increase in the friction factor and power consumption.

5.3. Comparison with previous studies

As shown in Fig. 17(a)(b)(c), the Nusselt number ratios, friction factor ratios and *EEC* of the present work are compared with that of previous works such as multiple regularly spaced twisted tapes [5], vortex rods [14], small pipe inserts [19], twisted-tapes [42], curved delta LVGs [43], conical strip inserts [44] and multiple conical strips inserts [45]. Compared with curved delta LVGs, conical stripe inserts and small pipes insert, the Nusselt number ratios of the present work are lower, but the friction factor ratios are much lower. The *EEC* is higher than most of previous works with $Re = 300–1500$ but lower than multiple conical stripes when Reynolds number is small.

5.4. Optimization calculation

5.4.1. Optimization objectives

Since the heat transfer and flow structure under a moderate Reynolds number have similarity to that under both small ($Re = 300$) and large Reynolds numbers ($Re = 1500$), it is typical to conduct optimization calculation with Reynolds number fixed to 900. The computational results for thermal dissipation and power consumption in the fully developed section are obtained for the optimization calculation. It is worth emphasizing that the periodic boundary condition is more suitable for obtaining the simulation data of fully developed section. The thermal dissipation owing to temperature differences and the power consumption owing to pressure drop are two contradictory objects in the tube. The optimization objectives are defined as Eqs. (24) and (25). The minus sign in Eq. (25) is to meet the requirements of the optimization algorithm.

$$Objective_1 = PCR = \frac{E_{xd,\Delta p}}{E_{xd,\Delta p,0}}, \tag{24}$$

$$Objective_2 = -TDR = -\frac{E_{xd,\Delta T,0}}{E_{xd,\Delta T}}. \tag{25}$$

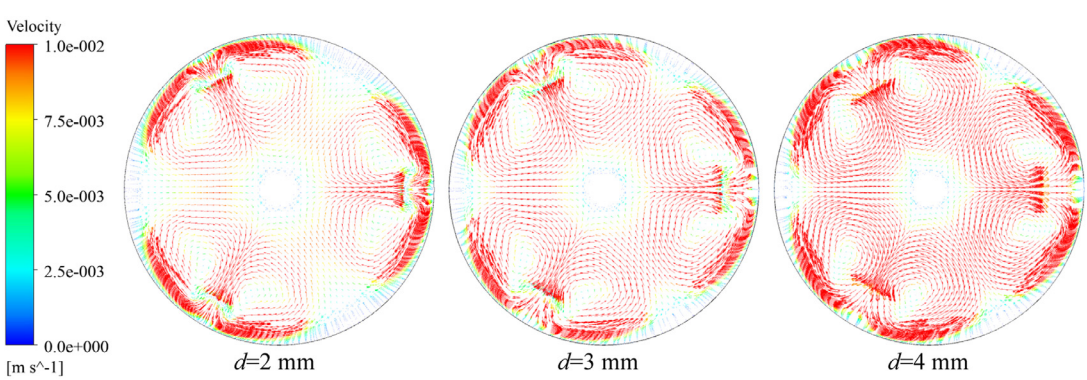

Fig. 16. Velocity distributions of cross sections under different deflector diameters at $Re = 900$, $\alpha = 30°$, $P = 40$ mm.

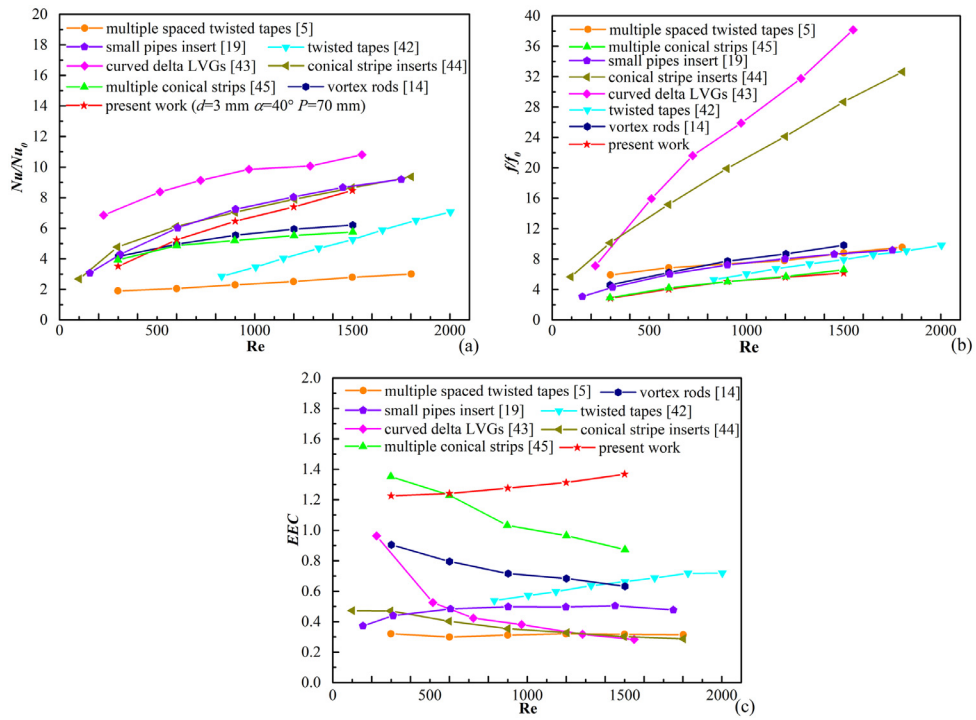

Fig. 17. Comparisons with previous works: (a) Nu/Nu_0, (b) f/f_0 and (c) *EEC*.

5.4.2. Optimization procedure

The optimization procedure [15,16], in which the *Re* is fixed to 900, is designed as follows. Firstly, five different values for inclined angle (α), pitch (P) and deflector diameter (d) are chosen respectively to obtain data base, which are displayed in Table 1. Thus, 125 ($5 \times 5 \times 5$) cases of parameter combination are calculated by the software of computational fluid dynamics (CFD for short). Secondly, considering a mass of workload in optimization calculation by the CFD method, the relationships between the inputs (α, P, and d) and the output ($Objective_1$ or $Objective_2$) are fitted with three-layer feed forward artificial neural networks (ANN for short) based on the computational results of above cases. Thirdly, the trained artificial neural networks work as objective functions in the genetic algorithm to conduct the multi-objective optimization. Finally, the Pareto front is obtained by the genetic algorithm and the final optimal parameters are determined according to the technique for order preference by similarity to the ideal solution (TOPSIS for short) [46]. The optimization procedure is illustrated in Fig. 18.

5.4.3. Fitting of the ANN

As shown in Fig. 19, the ANN consists of an input layer with three normalized neurons (α, P, and d), a hidden layer with several neurons, and an output layer with one neuron ($Objective_1$ or $Objective_2$). The training function and adaption learning function are default functions. The number of neurons in the hidden layer has a great influence on the ANN training results. Therefore, it is necessary to carry out an independence test for the number of neurons to ensure the accuracy of the ANN. The mean square error (*MSE* for short) and regression coefficient (*Reg* for short) are chosen as accuracy criteria, which are defined as:

$$MSE = \frac{1}{N}\sum_{i=1}^{N}(X_{i,ANN} - X_i)^2, \tag{26}$$

$$\mathrm{Reg} = \sqrt{1 - \sum_{i=1}^{N}\frac{(X_{i,ANN} - X_i)^2}{X_i^2}}. \tag{27}$$

A network with a smaller *MSE* and a larger *Reg* is regarded more reliable. Two artificial neural networks are trained for $Objective_1$ and $Objective_2$. The training results are listed in Table 3. According to the values of *MSE* and *Reg* in the table, the ANNs with eight neurons and nine neurons in the hidden layers are suitable for the power consumption ratio and the thermal dissipation ratio respectively, which are denominated as $net_{\Delta p}$ and $net_{\Delta T}$. Fig. 20 displays the deviations of the two dimensionless parameters between the results from the CFD and ANN. The maximum relative error is 5.7% for $net_{\Delta p}$ and 4.66% for $net_{\Delta T}$, respectively. Therefore, the ANNs meet the accuracy requirements.

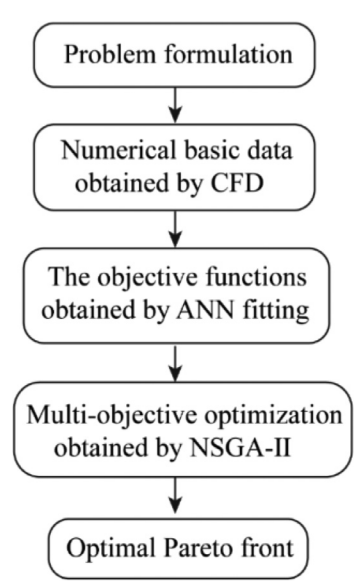

Fig. 18. Map of optimization procedure.

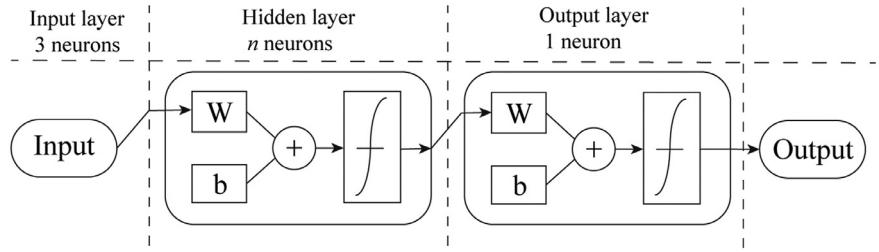

Fig. 19. Structure of neural network.

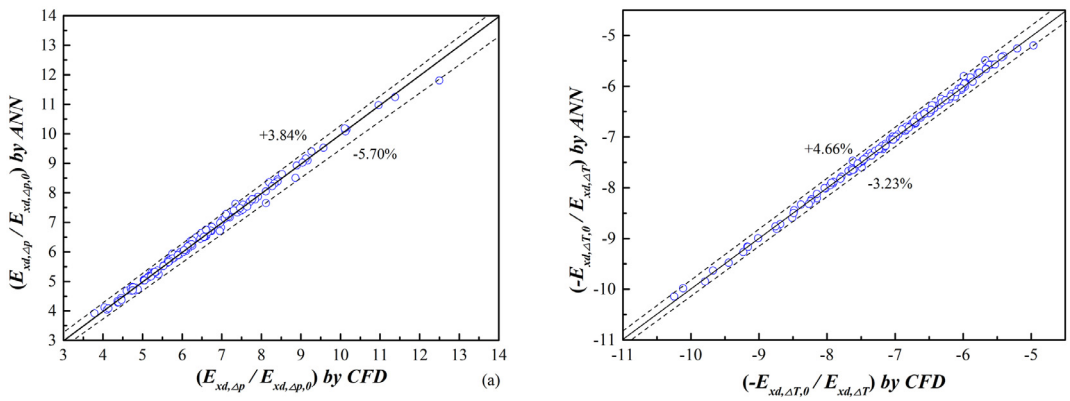

Fig. 20. Deviations between CFD simulation results and ANN fitting results.

Table 3
Neuron independence test.

Number of neurons	$net_{\Delta p}$		$net_{\Delta T}$	
	MSE	*Reg*	*MSE*	*Reg*
1	8.56E-04	0.98745	3.29E-03	0.95683
2	5.10E-04	0.99300	1.62E-03	0.98001
3	2.85E-04	0.99560	3.88E-04	0.99471
4	1.71E-04	0.99605	1.80E-04	0.99726
5	2.35E-04	0.99627	1.57E-04	0.99733
6	1.45E-04	0.99729	1.50E-04	0.99775
7	8.32E-05	0.99785	1.22E-04	0.99755
8	**2.23E-05**	**0.99846**	7.23E-05	0.99842
9	4.42E-05	0.99792	**2.27E-05**	**0.99895**
10	2.40E-05	0.99798	4.64E-05	0.99837
11	3.51E-05	0.99574	4.29E-05	0.99876
12	3.02E-05	0.99777	2.71E-05	0.99802
13	2.87E-05	0.99683	2.60E-05	0.99853
14	2.88E-05	0.99700	2.58E-05	0.99635
15	2.38E-05	0.99621	2.52E-05	0.99647

5.4.4. Results of multi-objective optimization

The multi-objective optimization can be described as follows:

Minimization: $f(\alpha, P, d) = \{E_{xd,\Delta p}/E_{xd,\Delta p,0}, -E_{xd,\Delta T,0}/E_{xd,\Delta T}\}$;
Subjected to: $\alpha \in [20, 60]$, $P \in [30, 70]$, $d \in [2, 4]$.

As mentioned in Section 5.4.1., the optimization objectives are determined as *Objective*$_1$ and *Objective*$_2$. Three geometrical parameters (α, P, and d) are the design variables. They are optimized according to the optimization objective minimization, which is guided by the principle of exergy destruction minimization. A fast non-dominated sorting genetic algorithm (NSGA for short) in the commercial software MATLAB is applied to perform the optimization and search the Pareto front. Two objective functions are defined according to $net_{\Delta p}$ and $net_{\Delta T}$ mentioned in Section 5.4.3. The design variables and their constraint conditions are listed in Table 4. The parameter setting for the NSGA are listed in Table 5.

Fig. 21 shows the Pareto front computed by the NSGA. In order to coordinate the heat transfer enhancement and increasing power

Table 4
Design variables and constraint conditions.

Design variables	Lower bound	Upper bound
α	20	60
P	30	70
d	2	4

Table 5
Parameter settings for NSGA-II.

Parameter	Value setting
Population size	100
Generation	500
Crossover fraction	0.8
Pareto factor	0.6
Function tolerance	10^{-4}

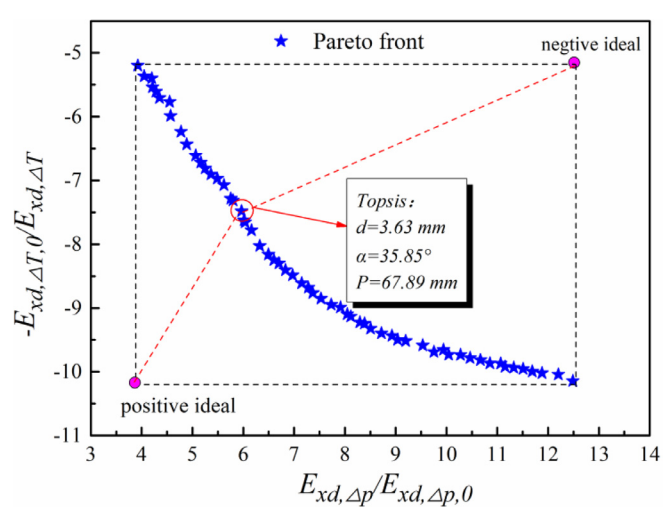

Fig. 21. Pareto front obtained by NSGA and a solution gained by TOPSIS method (Point A).

consumption and search a proper point for the active design of geometrical parameters of the insert, the technique for order preference by similarity to the ideal solution (TOPSIS for short) is applied. A solution at point A is gained, which has both the smallest geometric distance to positive ideal and the largest to negative ideal according to the properties of TOPSIS method [46]. For point A, the exergy destruction of heat transfer is decreased by 7.48 times while the exergy destruction of fluid flow is only increased by 5.69 times compared to the smooth tube, corresponding to optimal insert parameters of $d = 3.63$ mm, $\alpha = 35.85°$, and $P = 67.89$ mm.

In the Pareto front, Point B and C are two extreme solutions. The former one has minimal power consumption but maximal thermal dissipation, and the later one has minimal thermal dissipation but maximal power consumption. However, Point A, here, is a compromised solution on the Pareto front. Compared to point B, the thermal dissipation ratio at point A is deceased by 43.8% while the power consumption ratio is increased by 52.0%. Compared to point C, similarly, the thermal dissipation ratio at point A is increased by 26.1% while the power consumption ratio is deceased by 52.2%. The *EEC* value in point A of is 1.32, which is calculated by the CFD simulation based on above optimal insert parameters. It indicates that the principle of exergy destruction minimization can be applied to the active design for any insert in a heat transfer enhanced tube and that the overall performance of the optimized structure is considerable.

6. Conclusions

In summary, we can make the following conclusions for the present study.

(1) The longitudinal swirl flow and deflecting flow caused by the inserts simultaneously led to heat transfer enhancement in the tube. Within the calculation range considered, with $d = 2$–4 mm, $P = 30$–70 mm, $\alpha = 20$–$60°$ and $Re = 300$–1500, the Nusselt number of the present insert was increased by 2.51–9.46 times, while the friction factor was increased by 2.48–10.77 times. The value of *EEC* (efficiency evaluation criterion) was in the range of 0.92–1.56.

(2) The exergy destructions induced by temperature difference and pressure drop were reflected by the thermal dissipation and power consumption of the fluid respectively. Compared with the smooth tube, the thermal dissipation was decreased by 4.82–10.56 times, while the power consumption was increased by 3.78–12.50 times in the enhanced tube within the calculation range considered.

(3) The effects of the *Re* number and geometrical parameters of the insert including the pitch (P), inclined angle (α) and deflector diameter (d) on the thermo-hydraulic characteristics were demonstrated. With the decreasing in smaller pitch or increasing in deflector diameter, inclined angle and Reynold number, Nusselt number, friction factor and power consumption increased while thermal dissipation decreased.

(4) The optimization, in which the exergy destructions caused by both heat transfer and fluid flow were chosen as the optimization objectives, was performed by the NSGA along with the ANN to collaboratively minimize the two objectives, and the Pareto front reflecting the thermal dissipation and power consumption ratios of the fluid was obtained. A compromised solution ($d = 3.63$ mm, $\alpha = 35.85°$, and $P = 67.89$ mm) was found by the TOPSIS method, and the *EEC* in the enhanced tube of this solution was 1.32. Thus, in this paper, an active design method for the tube insert was put forward based on the principle of energy destruction minimization.

Declaration of Competing Interest

The authors do not have any possible conflicts of interest.

CRediT authorship contribution statement

J.Y. Lv: Methodology, Software, Validation, Formal analysis, Writing - original draft, Writing - review & editing, Visualization. **Z.C. Liu:** Conceptualization, Writing - review & editing, Supervision, Project administration, Funding acquisition. **W. Liu:** Conceptualization, Writing - review & editing, Supervision, Project administration, Funding acquisition.

Acknowledgment

This work was supported by the National Natural Science Foundation of China (grant no. 51736004).

Supplementary materials

Supplementary material associated with this article can be found, in the online version, at doi:10.1016/j.ijheatmasstransfer.2019.119260.

References

[1] S. Liu, M. Sakr, A comprehensive review on passive heat transfer enhancements in pipe exchangers, Renew. Sustain. Energy Rev. 19 (2013) 64–81.
[2] A.M. Abed, M.A. Alghoul, M.H. Yazdi, A.N. Al-Shamani, K. Sopian, The role of enhancement techniques on heat and mass transfer characteristics of shell and tube spray evaporator: a detailed review, Appl. Therm. Eng. 75 (2015) 923–940.
[3] P. Pongsoi, S. Pikulkajorn, S. Wongwises, Heat transfer and flow characteristics of spiral fin-and-tube heat exchangers: A review, Int. J. Heat Mass Transf. 79 (2014) 417–431.
[4] Y. He, L. Liu, P. Li, L. Ma, Experimental study on heat transfer enhancement characteristics of tube with cross hollow twisted tape inserts, Appl. Therm. Eng. 131 (2018) 743–749.
[5] X. Zhang, Z. Liu, W. Liu, Numerical studies on heat transfer and flow characteristics for laminar flow in a tube with multiple regularly spaced twisted tapes, Int. J. Therm. Sci. 58 (2012) 157–167.
[6] J. Guo, A. Fan, X. Zhang, W. Liu, A numerical study on heat transfer and friction factor characteristics of laminar flow in a circular tube fitted with center–cleared twisted tape, Int. J. Therm. Sci. 50 (7) (2011) 1263–1270.
[7] A. Saysroy, S. Eiamsa-ard, Periodically fully-developed heat and fluid flow behaviors in a turbulent tube flow with square-cut twisted tape inserts, Appl. Therm. Eng. 112 (2017) 895–910.
[8] Z. Feng, X. Luo, F. Guo, H. Li, J. Zhang, Numerical investigation on laminar flow and heat transfer in rectangular microchannel heat sink with wire coil inserts, Appl. Therm. Eng. 116 (2017) 597–609.
[9] S. Gunes, V. Ozceyhan, O. Buyukalaca, Heat transfer enhancement in a tube with equilateral triangle cross sectioned coiled wire inserts, Exp. Therm. Fluid Sci. 34 (6) (2010) 684–691.
[10] O. Turgut, E. Kizilirmak, Effects of Reynolds number, baffle angle, and baffle distance on three-dimensional turbulent flow and heat transfer in a circular pipe, Therm. Sci. 19 (5) (2015) 1633–1648.
[11] S.W. Chang, T.W. Chen, Y.W. Chen, Detailed heat transfer and friction factor measurements for square channel enhanced by plate insert with inclined baffles and perforated slots, Appl. Therm. Eng. (2019) 159.
[12] B. Kotresha, N. Gnanasekaran, Determination of interfacial heat transfer coefficient for the flow assisted mixed convection through brass wire mesh, Int. J. Therm. Sci. 138 (2019) 98–108.
[13] W. Tu, Y. Wang, Y. Tang, J. Xu, Heat transfer and pressure drop characteristics in a circular tube with mesh cylinder inserts, Int. Commun. Heat Mass Transfer 75 (2016) 130–136.
[14] N. Zheng, P. Liu, F. Shan, J. Liu, Z. Liu, W. Liu, Numerical studies on thermo-hydraulic characteristics of laminar flow in a heat exchanger tube fitted with vortex rods, Int. J. Therm. Sci. 100 (2016) 448–456.
[15] A. Abdollahi, M. Shams, Optimization of shape and angle of attack of winglet vortex generator in a rectangular channel for heat transfer enhancement, Appl. Therm. Eng. 81 (2015) 376–387.
[16] N. Zheng, P. Liu, X. Wang, F. Shan, Z. Liu, W. Liu, Numerical simulation and optimization of heat transfer enhancement in a heat exchanger tube fitted with vortex rod inserts, Appl. Therm. Eng. 123 (2017) 471–484.
[17] Y. Wang, P. Liu, F. Shan, Z. Liu, W. Liu, Effect of longitudinal vortex generator on the heat transfer enhancement of a circular tube, Appl. Therm. Eng. 148 (2019) 1018–1028.
[18] A.W. Fan, J.J. Deng, A. Nakayama, W. Liu, Parametric study on turbulent heat transfer and flow characteristics in a circular tube fitted with louvered strip inserts, Int. J. Heat Mass Transf. 55 (19-20) (2012) 5205–5213.

[19] W. Tu, Y. Tang, J. Hu, Q. Wang, L. Lu, Heat transfer and friction characteristics of laminar flow through a circular tube with small pipe inserts, Int. J. Therm. Sci. 96 (2015) 94–101.
[20] Y.-L. He, W.-Q. Tao, Numerical studies on the inherent interrelationship between field synergy principle and entransy dissipation extreme principle for enhancing convective heat transfer, Int. J. Heat Mass Transf. 74 (2014) 196–205.
[21] Q. Wang, M. Zeng, T. Ma, X. Du, J. Yang, Recent development and application of several high-efficiency surface heat exchangers for energy conversion and utilization, Appl. Energy 135 (2014) 748–777.
[22] W. Tu, Y. Wang, Y. Tang, Thermal characteristic of a tube fitted with porous media inserts in the single phase flow, Int. J. Therm. Sci. 110 (2016) 137–145.
[23] Y.H. Said, On genetic algorithms and their applications, in: Data Mining and Data Visualization, 2005, pp. 359–390.
[24] S.F. Ding, C.Y. Su, J.Z. Yu, An optimizing BP neural network algorithm based on genetic algorithm, Artif. Intell. Rev. 36 (2011) 153–162.
[25] A. Bejan, Entropy Generation Minimization, John Wiley & Sons, New York, 1995.
[26] A. Bejan, Entropy generation minimization: The new thermodynamics of finite-size devices and finite-time processes, J. Appl. Phys. 79 (3) (1996) 1191–1218.
[27] Z.-Y. Guo, H.-Y. Zhu, X.-G. Liang, Entransy—A physical quantity describing heat transfer ability, Int. J. Heat Mass Transfer 50 (13-14) (2007) 2545–2556.
[28] Q. Chen, X.-G. Liang, Z.-Y. Guo, Entransy theory for the optimization of heat transfer–A review and update, Int. J. Heat Mass Transf. 63 (2013) 65–81.
[29] T. Zhao, D. Liu, Q. Chen, A collaborative optimization method for heat transfer systems based on the heat current method and entransy dissipation extremum principle, Appl. Therm. Eng. 146 (2019) 635–647.
[30] W. Wang, X. Cheng, X. Liang, Entropy and entransy analyses and optimizations of the Rankine cycle, Energy Convers. Manage. 68 (2013) 82–88.
[31] Z.Y. Guo, W.Q. Tao, R.K. Shah, The field synergy (coordination) principle and its applications in enhancing single phase convective heat transfer, Int. J. Heat Mass Transf. 48 (9) (2005) 1797–1807.
[32] Q. Chen, J. Ren, J.-a. Meng, Field synergy equation for turbulent heat transfer and its application, Int. J. Heat Mass Transf. 50 (25-26) (2007) 5334–5339.
[33] Y.L. He, W.Q. Tao, F.Q. Song, W. Zhang, Three-dimensional numerical study of heat transfer characteristics of plain plate fin-and-tube heat exchangers from view point of field synergy principle, Int. J. Heat Fluid Flow 26 (3) (2005) 459–473.
[34] Y.B. Tao, Y.L. He, Z.G. Wu, W.Q. Tao, Three-dimensional numerical study and field synergy principle analysis of wavy fin heat exchangers with elliptic tubes, Int. J. Heat Fluid Flow 28 (6) (2007) 1531–1544.
[35] W. Liu, P. Liu, Z.M. Dong, K. Yang, Z.C. Liu, A study on the multi-field synergy principle of convective heat and mass transfer enhancement, Int. J. Heat Mass Transfer 134 (2019) 722–734.
[36] L. Wei, L. Zhichun, M. Tingzhen, G. Zengyuan, Physical quantity synergy in laminar flow field and its application in heat transfer enhancement, Int. J. Heat Mass Transf. 52 (19-20) (2009) 4669–4672.
[37] W. Liu, Z. Liu, L. Ma, Application of a multi-field synergy principle in the performance evaluation of convective heat transfer enhancement in a tube, Chin. Sci. Bull. 57 (13) (2012) 1600–1607.
[38] W. Liu, J.B. Wang, Z.C. Liu, A method of fluid dynamic analysis based on Navier-Stokes equation and conservation equation on fluid mechanical energy, Int. J. Heat Mass Transf. 109 (2017) 393–396.
[39] Y. Cao, H. Ke, Q. Wang, et al., Investigation on the flow noise propagation mechanism in simple expansion pipelines based on synergy principle of flow and sound fields, Energy Procedia. 142 (2017) 3870–3875.
[40] W. Liu, P. Liu, J.B. Wang, N.B. Zheng, Z.C. Liu, Exergy destruction minimization: A principle to convective heat transfer enhancement, Int. J. Heat Mass Transf. 122 (2018) 11–21.
[41] J. Wang, W. Liu, Z. Liu, The application of exergy destruction minimization in convective heat transfer optimization, Appl. Therm. Eng. 88 (2015) 384–390.
[42] K. Wongcharee, S. Eiamsa-ard, Friction and heat transfer characteristics of laminar swirl flow through the round tubes inserted with alternate clockwise and counter-clockwise twisted-tapes, Int. Commun. Heat Mass Transf. 38 (3) (2011) 348–352.
[43] P.W. Deshmukh, S.V. Prabhu, R.P. Vedula, Heat transfer enhancement for laminar flow in tubes using curved delta wing vortex generator inserts, Appl. Therm. Eng. 106 (2016) 1415–1426.
[44] Y. You, A. Fan, W. Liu, S. Huang, Thermo-hydraulic characteristics of laminar flow in an enhanced tube with conical strip inserts, Int. J. Therm. Sci. 61 (2012) 28–37.
[45] P. Liu, N. Zheng, F. Shan, Z. Liu, W. Liu, An experimental and numerical study on the laminar heat transfer and flow characteristics of a circular tube fitted with multiple conical strips inserts, Int. J. Heat Mass Transf. 117 (2018) 691–709.
[46] L Hwang C, K Yoon, Multiple attribute decision making: methods and applications, Springer, New York, 1981.